

Multi-Scale Pipeline for the Search of String-Induced CMB Anisotropies

A. Vafaei Sadr^{1,2,3}, S. M. S. Movahed^{1,4*}, M. Farhang¹, C. Ringeval⁵, F. R. Bouchet⁶

¹*Department of Physics, Shahid Beheshti University, Velenjak, Tehran 19839, Iran*

²*Département de Physique Théorique and Center for Astroparticle Physics, Université de Genève, 24 Quai Ernest Ansermet, 1211 Genève 4, Switzerland*

³*African Institute for Mathematical Sciences, 6 Melrose Road, Muizenberg, 7945, South Africa*

⁴*School of Physics, Institute for Research in Fundamental Sciences (IPM), P. O. Box 19395-5531, Tehran, Iran*

⁵*Centre for Cosmology, Particle Physics and Phenomenology, Université Catholique de Louvain, Louvain-la-Neuve B-1348, Belgium*

⁶*Institut d'Astrophysique de Paris (UMR7095: CNRS & UPMC-Sorbonne Universities), F-75014, Paris, France*

28 August 2018

ABSTRACT

We propose a multi-scale edge-detection algorithm to search for the Gott-Kaiser-Stebbins imprints of a cosmic string (CS) network on the Cosmic Microwave Background (CMB) anisotropies. Curvelet decomposition and extended Canny algorithm are used to enhance the string detectability. Various statistical tools are then applied to quantify the deviation of CMB maps having a cosmic string contribution with respect to pure Gaussian anisotropies of inflationary origin. These statistical measures include the one-point probability density function, the weighted two-point correlation function (TPCF) of the anisotropies, the unweighted TPCF of the peaks and of the up-crossing map, as well as their cross-correlation. We use this algorithm on a hundred of simulated Nambu-Goto CMB flat sky maps, covering approximately 10% of the sky, and for different string tensions $G\mu$. On noiseless sky maps with an angular resolution of $0.9'$, we show that our pipeline detects CSs with $G\mu$ as low as $G\mu \gtrsim 4.3 \times 10^{-10}$. At the same resolution, but with a noise level typical to a CMB-S4 phase II experiment, the detection threshold would be to $G\mu \gtrsim 1.2 \times 10^{-7}$.

Key words: cosmic background radiation - cosmology; theory - early Universe - large-scale structure of Universe.

1 INTRODUCTION

The inflationary Λ CDM model with nearly Gaussian and scale-invariant primordial density perturbations has been confirmed with high precision as a robust cosmological model thanks in particular to the observations of the cosmic microwave background radiation (CMB) (Hinshaw et al. 2013; Ade et al. 2016). The initial conditions for the large-scale structure of the Universe, determined by primordial cosmological perturbations are seeded by quantum fluctuations of a scalar field during the so-called inflationary epoch (Guth 1981; Liddle & Lyth 1993; Steinhardt 1995; Liddle 1999). Despite the outstanding agreement between the standard model and the cosmic data, there is some limited room for alternative scenarios as well. One such scenario is to consider topological defects as minor contributors to the primordial perturbations. Many quantum field theories typically predict these defects as a result of phase transition caused by

spontaneous breaking of their symmetries due to the expansion and cooling of the Universe (Kibble 1976, 1980; Hindmarsh & Kibble 1995; Vilenkin & Shellard 2000; Copeland & Kibble 2010; Polchinski 2005).

The line-like version of topological defects are called cosmic strings (CSs) and are commonly present in theories of hybrid inflation, brane-world models and superstring theory (Kibble 1976; Zeldovich 1980; Vilenkin 1981; Vachaspati & Vilenkin 1984; Vilenkin 1985; Shellard 1987; Hindmarsh & Kibble 1995; Vilenkin & Shellard 2000; Sakellariadou 2007; Bevis et al. 2008; Depies 2009; Bevis et al. 2010; Copeland et al. 1994; Sakellariadou 1997; Sarangi & Tye 2002; Copeland et al. 2004; Pogosian et al. 2003; Majumdar & Christine-Davis 2002; Dvali & Vilenkin 2004; Kibble 2004; Henry Tye 2008). They represent lines of trapped energy density parameterized by $G\mu$. G is Newton's constant and μ represents the mass per unit length of the string, also equal to its tension. The string tension is closely related to

* E-mail: m.s.movahed@ipm.ir

the energy of the symmetry breaking scale, ϖ , as:

$$\frac{G\mu}{c^2} = \mathcal{O}\left(\frac{\varpi^2}{M_{\text{Planck}}^2}\right). \quad (1)$$

here $M_{\text{Planck}} \equiv \sqrt{\hbar c/G}$ represents the Planck's mass and c is the speed of light. In this paper we choose to work in natural units with $\hbar = c = 1$. Symmetry breaking at energies around the GUT scale would thus correspond to production of CSs with $G\mu \sim 10^{-6}$ (Kibble 1976; Zeldovich 1980; Vilenkin 1981; Vilenkin & Shellard 2000; Firouzjahi & Tye 2005). Therefore, CS studies provide a unique path to the physics of extremely high energies far beyond the access of our Earth-bound laboratories. The evolution of a network of CSs, containing loops, long strings and their junctions, depends not only on the string tension, but also on the equation of motion of the strings, the initial conditions and the string inter-commutation probability, that represents the probability of their collisions, (Vachaspati & Vilenkin 1984; Ringeval et al. 2007; Blanco-Pillado et al. 2011).

The search for CSs takes different theoretical, statistical and observational routes, thanks to their diverse imprints on cosmological data sets. These searches have led to constraints on $G\mu$, which is the main free parameter characterizing CSs. For example, recent results from the gravitational wave emission of Nambu-Goto cosmic string loops constrain the CS tension to be $10^{-14} \leq G\mu \leq 1.5 \times 10^{-10}$ depending on the string microstructure (Ringeval & Suyama 2017; Blanco-Pillado & Olum 2017; Blanco-Pillado et al. 2017). Pulsar timing and photometry, based on gravitational microlensing, constrain CS's tension to $10^{-15} < G\mu < 10^{-8}$ (Jenet et al. 2006; Pshirkov & Tuntsov 2010; Tuntsov & Pshirkov 2010; Damour & Vilenkin 2005; Battye & Moss 2010; Oknyanskij 2002; Kuroyanagi et al. 2013). The upper bound of $G\mu < 3 \times 10^{-7}$ has also been reported by the COSMOS survey (Christiansen et al. 2011). The 21-cm signature of CS wakes has also been theoretically explored in Brandenberger et al. (2010); Hernandez et al. (2011); Hernandez & Brandenberger (2012); Pagano & Brandenberger (2012) and forecasts have been made on how strongly these near-future surveys would measure $G\mu$. On the other hand, Schlaer et al. (2012) have studied signature of CSs on high-redshift large-scale structure surveys and on the ionization history of the Universe.

The CS network, if it exists, should have also left unique imprints on CMB anisotropies. Their integrated Sachs-Wolfe (ISW) contribution, also known as the Gott-Kaiser-Stebbins effect (Kaiser & Stebbins 1984; Gott III 1985; Stebbins 1988; Bouchet et al. 1988; Allen et al. 1997; Pen et al. 1997), is primarily caused by the transverse motion of the CSs with respect to the observer. The resulting energy shift of CMB photons produces line-like discontinuities on CMB anisotropies at the string location such that, in the light-cone gauge, one has (Kaiser & Stebbins 1984; Gott III 1985; Hindmarsh 1994; Stebbins & Veeraraghavan 1995)

$$\frac{\delta T}{T} \sim 8\pi G\mu v_s, \quad (2)$$

where v_s is the transverse velocity of the string.

Simulating the impact of the CS network on CMB anisotropies requires various simplifying assumptions. The models used in the literature generally fall in one of the followings:

(i) Nambu-Goto simulations (Bennett & Bouchet 1988, 1989; Bouchet et al. 1988; Landriau & Shellard 2003, 2004; Fraisse et al. 2008; Ringeval & Bouchet 2012), (ii) using stochastic ensemble of unconnected segments (Allen et al. 1997; Albrecht et al. 1997; Contaldi et al. 1999; Pogosian & Vachaspati 1999; Pogosian et al. 2006), (iii) Abelian-Higgs model on a lattice, with the evolution of the network determined by the corresponding fields (Vincent et al. 1998; Moore et al. 2002; Kasuya & Kawasaki 2000; Bevis et al. 2007), and (iv) the so-called statistical approach, explained below (Perivolaropoulos 1993a,b; Moessner et al. 1994; Jeong & Smoot 2005; Amsel et al. 2008; Stewart & Brandenberger 2009; Danos & Brandenberger 2010; Movahed & Khosravi 2011).

The (i) – (iii) approaches solve the photon propagation at linear order within a CS simulation network to get CMB fluctuations. Previous results from these models showed that at intermediate and small scales, topological defects and inflationary models lead to completely different results, while at large enough scales both scenarios result in similar features in the CMB power spectrum. The fourth method uses the number of random kicks on photon trajectories by CSs network between the time of recombination and the present era. This approach requires dealing with analytical and numerical tools and is explained in detail in Stewart & Brandenberger (2009); Danos & Brandenberger (2010); Movahed & Khosravi (2011).

To measure the contribution of CSs to the CMB power spectrum, the standard parameter estimation techniques are extended to include a new parameter, usually denoted by f_{10} , quantifying the fraction of the power at $\ell = 10$ due to strings. The incoherency of the perturbations produced by the strings as active sources leads to a significantly broad peak compared to the relatively sharp peak from the standard acoustic oscillations. The measurements of the CMB power spectrum leave limited space for contribution from CS-induced perturbations (Pen et al. 1997; Bevis et al. 2007, 2010; Lazanu & Shellard 2015). The *Planck* data (Ade et al. 2014) constrains this contribution to be $f_{10} < 0.024$ (corresponding to $G\mu < 3.0 \times 10^{-7}$) for Abelian-Higgs strings and $f_{10} < 0.010$ (corresponding to $G\mu < 1.3 \times 10^{-7}$) for unconnected segments. Adding CMB polarization improves the upper bound to $G\mu < 1.1 \times 10^{-7}$ (Charnock et al. 2016). Latest results for Nambu-Goto strings give an upper bound of $G\mu < 1.5 \times 10^{-7}$ from the *Planck* data with polarization (Lazanu & Shellard 2015). One should note though that *Planck* 15 polarization data is preliminary at large multipoles due to residual systematics at the $\mathcal{O}(1\mu K^2)$ level.

An alternative approach to constrain $G\mu$ is based on the non-Gaussianity of CS-induced fluctuations (Ringeval 2010; Ducout et al. 2013). For example, bispectrum measurement of the observed CMB anisotropies, Wavelet-based data analysis methods and measurements of the Minkowski functionals of the CMB data have set the upper bounds of $G\mu < 8.8 \times 10^{-7}$, $G\mu < 7 \times 10^{-7}$ and $G\mu < 7.8 \times 10^{-7}$, respectively (Hindmarsh et al. 2009, 2010; Ade et al. 2014; Regan & Hindmarsh 2015).

On the other hand, the discontinuities on the CMB anisotropy maps produced by the CS network most clearly manifest themselves in the real-space approaches. These methods are expected to be less time consuming compared to Fourier-based approaches. Among the real-space methods

with strings modeled as random kicks (Movahed & Khosravi 2011) used the crossing statistics of simulated ideal CMB fluctuations and claimed detectability of CSs with $G\mu \gtrsim 4.0 \times 10^{-9}$. Using the unweighted Two-Point Correlation Function (TPCF) of CMB peaks instead increases the detectability threshold to $G\mu \gtrsim 1.2 \times 10^{-8}$ for noiseless, $1'$ -resolution maps (Movahed et al. 2012).

Another potentially powerful method in real-space analysis is to exploit our knowledge of the anisotropy patterns from CSs, i.e., the line-like edges. (Stewart & Brandenberger 2009) applied edge-detection algorithms on ideal random-kick maps to get a detection threshold of $G\mu \gtrsim 5.5 \times 10^{-8}$ for the South Pole Telescope (SPT). Using wavelet and curvelet methods, (Hergt et al. 2016) found a sensitivity of $G\mu \gtrsim 1.4 \times 10^{-7}$ for the SPT third generation. Recently, neural network-based approaches have been applied by (Ciuca & Hernández 2017) on noiseless arcminute-resolution random-kick maps to reach a detection threshold of $G\mu \gtrsim 5 \times 10^{-9}$.

The different values reported above are, in part, the results of the crude assumptions made to model the strings. For this reason, in the following, we will be using small angle CMB maps directly computed from Nambu-Goto simulations (Ringeval et al. 2007; Fraisse et al. 2008; Ringeval & Bouchet 2012). In particular, these maps are the flat version of the ones recently used by (McEwen et al. 2016) which reported a Bayesian detection threshold of $G\mu \sim 5 \times 10^{-7}$ for a *Planck*-like CMB experiment. This allows a fair comparison with our results for the *Planck*-like CMB maps (see section 4). For forthcoming arcminute-resolution experiments (Hammond et al. 2009) used wavelet-domain Bayesian denoising on two of the maps we have used to obtain the detection lower bound of $G\mu \geq 1.0 \times 10^{-7}$.

In this work, we develop a new pipeline to search for the CS signals. Taking the CMB map as the input, the pipeline follows several image processing steps to enhance the detectability of the CS trace. More specifically, the CMB map is decomposed into various curvelet components, with different scales, so that only components with the highest contribution from CSs are kept for further analysis. These components are then passed through certain filters to produce gradient maps thereby boosting the CS-induced discontinuities. At the last step of the pipeline, various statistical measures are applied on the gradient maps to quantify possible deviations from inflation-induced anisotropies.

Our proposed pipeline has certain degrees of freedom which set its adjustable parameters such as the curvelet component to be used, the filter type in the edge-detection step, and the kind of the statistical measure to be applied on the gradient maps. For each experimental setup, the pipeline automatically searches for the optimum sequence of parameters yielding the tightest constraint on the CS contribution.

The outline of this paper is as follows. In Section 2, we introduce the different components of our CMB simulations. Section 3 describes in details our proposed pipeline for CS detection, and in Section 4, we present the performance of the pipeline by applying it on simulated CMB data with various noise levels. We conclude in Section 5.

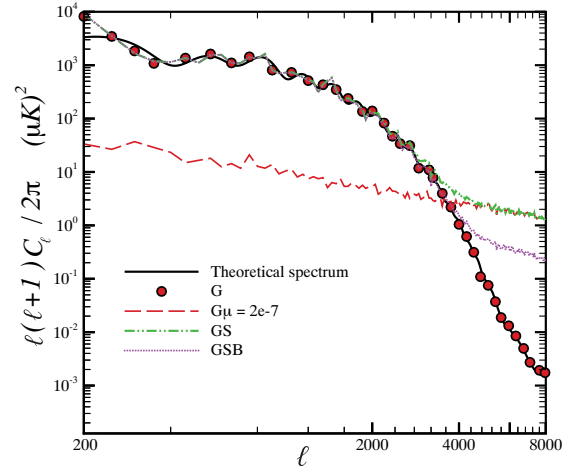


Figure 1. The CMB power spectrum: the black solid line shows the fiducial power spectrum for the Λ CDM model compatible with *Planck* 15 (Aghanim et al. 2016) (computed by CAMB). The red filled circles represent the measured power spectrum of simulated Gaussian maps seeded only by inflationary fluctuations, with pixel resolution of $R = 0.42'$ and map size of $\Theta = 7.2^\circ$. The red long-dashed line shows the contribution to the power spectrum from CS network characterized by $G\mu = 2.0 \times 10^{-7}$. The dashed-dotted curve corresponds to the measured power spectrum of CMB maps including both inflationary and CS-induced anisotropies. The dotted curve corresponds to the measured power spectrum of maps smeared by the beam (Section 2.4). One sees that, in the absence of noise and other small scale contaminations, the CS component is most easily detected at $\ell \gtrsim 4000$.

2 SIMULATION OF CMB MAPS

In this section, we describe the details of our simulations for making CMB sky maps, used in Section 4 to investigate the detectability of the string contribution to the CMB anisotropies. The simulations consist of three components: (1) the Gaussian inflation-induced contribution denoted by G , as well as the secondary lensing signal (Section 2.1), (2) the CS contribution, $G\mu \times S$, where S represents the normalized simulated template for the string signal and $G\mu$ sets its amplitude (Section 2.2), and (3) the experimental noise indicated by N (section 2.3). The full simulated map $T(x, y)$, with x and y representing pixel coordinates, would then be

$$T(x, y) = B [G(x, y) + G\mu \times S(x, y)] + N(x, y). \quad (3)$$

where B characterizes the beam function (Section 2.4). In the figures throughout this paper, we use G for Gaussian simulated map, S for the CS-induced anisotropy map and N for the noise map. For example, GSB refers to simulations with all components included, with B representing the beam effect. We work in the flat sky limit (Heavens & Sheth 1999) with 100 square maps of side $\Theta = 7.2^\circ$, with 1024×1024 pixels. This corresponds to a resolution of $R = 0.42'$ before convolution with an experimental beam. We also assume statistical isotropy in all our simulations.

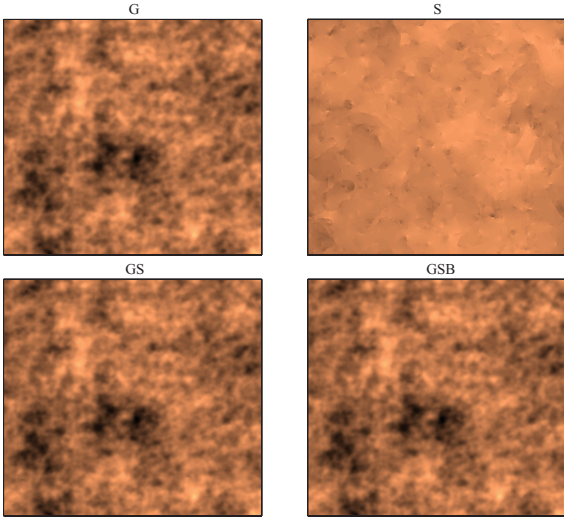


Figure 2. Different components of our simulated maps. The map size is $7.2^\circ \times 7.2^\circ$ at resolution $R = 0.42'$. The upper left plot is a Gaussian CMB map, named by G in the text, simulated based on *Planck* 15 Λ CDM parameters. The upper right plot shows the CS-induced anisotropies, i.e., the S component, with $G\mu = 2.0 \times 10^{-7}$. The lower left panel is the combination of the two, i.e., the GS map, smeared by the beam (Section 2.4) in the lower right panel, making the GSB map.

2.1 Gaussian CMB simulation

The Gaussian component of CMB temperature anisotropies is assumed to be seeded by adiabatic scale-invariant slow-roll-inflationary fluctuations. The only secondary contribution considered here is due to lensing. To this end, we use the CAMB software¹ (Lewis et al. 2000) to calculate the temperature power spectrum for the parameter set of the Λ CDM model consistent with *Planck* 15, Supernova type Ia (SNIa) and the Sloan Digital Sky Survey (SDSS) data sets (Aghanim et al. 2016). The computed C_ℓ will be used to generate 2D Gaussian random fields following (Bond & Efstathiou 1987). The maps $G(x, y)$ are generated by Fourier-transforming Gaussian random realizations $G(\mathbf{k})$ of CMB temperature power spectrum in the flat sky limit $P_{TT}(k)$,

$$G(\mathbf{k}) = \sqrt{\frac{P_{TT}(k)}{2}} (\mathcal{R}_1 + i\mathcal{R}_2), \quad (4)$$

where \mathcal{R}_1 and \mathcal{R}_2 are two mean-less unit variance normal random fields, and $k = |\mathbf{k}|$. For the flat power spectrum $P_{TT}(k)$ one has $\langle \delta_T(\mathbf{k}) \delta_T^*(\mathbf{k}') \rangle = (2\pi)^2 P_{TT}(k) \delta_d(\mathbf{k} - \mathbf{k}')$, where δ_d denotes the Dirac delta function. $P_{TT}(k)$ is related to the full sky power spectrum through $\ell(\ell+1)C_\ell^{TT} \sim k^2 P_{TT}(k)$ (White et al. 1999; Hindmarsh et al. 2009; Fraisse et al. 2008).

Figure 1 compares the fiducial power spectrum as produced by CAMB (the solid black line) with the measured power spectrum from the simulated Gaussian maps (the filled circle symbols). Figure 2 illustrates various contributions to the simulations and their combinations.

¹ <http://camb.info>

2.2 Cosmic string simulation

For the CS-induced CMB anisotropies, we use 100 high-resolution flat-sky CMB maps identical to the ones discussed by (Fraisse et al. 2008). They are obtained from numerical simulations of Nambu-Goto string networks using the Bennett-Bouchet-Ringeval code (Bennett & Bouchet 1990; Ringeval et al. 2007) together with a direct computation of the ISW effect generated by each string along the line of sight. Unlike other numerical methods which are restricted to a short redshift span, typically $\Delta z \approx 10^2$, and are thus only reliable on large angular scales, these simulations are produced by stacking maps from various redshifts (outlined in Bouchet et al. 1988; Ringeval & Bouchet 2012), a valid approach for small scale simulations. Among the main simplifying assumptions used in these simulations is the small-angle approximation used in the computation of the ISW effect from CSs (Stebbins 1988; Hindmarsh 1994; Stebbins & Veeraraghavan 1995).

The CS-induced anisotropies with the desired amplitude and the inflationary Gaussian anisotropies are then combined to form our CMB sky, without yet the instrumental effects being taken into account. The CS tensions used in this work are in the range $2.6 \times 10^{-11} \leq G\mu \leq 5.0 \times 10^{-7}$. One can therefore ignore the effect of string contribution on the CMB power spectrum in the scales of interest in our analysis, without losing much precision. This can be seen from Figure 1. The long-dashed line represents the power spectrum C_ℓ^s of CS contribution to the fluctuations, expected to behave as $\ell(\ell+1)C_\ell^s \sim \ell^{-\varepsilon}$ with $\varepsilon = 0.90 \pm 0.05$ for $\ell \gg 1$ (Fraisse et al. 2008). A map of CMB anisotropies generated by a CS network with $G\mu = 2.0 \times 10^{-7}$ is illustrated in the upper right panel of Figure 2, compared to the GS-realization (lower left panel). Careful visual investigation of the plots reveals noticeable sharp edges from string anisotropies.

2.3 Instrumental noise

Our model of the instrumental noise is a white Gaussian random field characterized by the signal-to-noise ratio SNR , taken to be 10, 15 and 20. These noise levels are close to the instrumental noise of the Atacama Cosmology Telescope (ACT), CMB-S4 phase I and CMB-S4 phase II, respectively. The goal here is to see the overall impact of noise contamination on the CS detectability. It is obvious that making realistic forecast of the capability of any experiment in the search for the CSs would require more realistic noise modeling.

2.4 Beam

Due to the finite resolution of the telescopes, observed CMB temperature anisotropies are the result of the convolution of underlying temperature distribution on the sky with the instrumental beam. In the following, we consider two types of experiment. The first is a *Planck*-like experiment in which the beam is modeled as a Gaussian with FWHM = $5'$. This is the beam used for the *Planck*-like observational setup in this work. Based on the specification of the Millimeter Biometric Array Camera (MBAC) generation of CMB detectors used in ACT, a second type of beam is used for any other experimental strategy (i.e., the ACT-like, the CMB-S4 phase I-

and II-like and the ideal, noise-free experiments). We select the effective band center 274 GHz with FWHM = 0.9'.

Following the notation of (Fraisse et al. 2008), the Fourier components of the observed CMB map, $\mathcal{V}(k)$, will be described by

$$\mathcal{V}(k) = \frac{\partial B_\nu(T)}{\partial T} T_{\text{CMB}} \int \delta_T(r) A(r) e^{-i\mathbf{k}\cdot\mathbf{r}} d^2r. \quad (5)$$

Here, k is the wave-number and \mathbf{r} is the coordinate of a point on the telescope. Also $\delta_T(r)$, $B_\nu(T)$ and $A(r)$ represent respectively the CMB temperature anisotropy on the sky, the *Planck* function and the primary beam function, here taken to have an Airy pattern. In the simulations, we use the Fourier transform of the beam per unit area, $\tilde{A}(u)$, related to the beam itself through

$$A(r) = \frac{1}{(2\pi)^2} \int \tilde{A}(u) e^{2\pi i(\mathbf{u}\cdot\mathbf{r})} d^2u. \quad (6)$$

with

$$\tilde{A}(u) = \mathcal{A} \left[\arccos \frac{u}{u_c} - \frac{u}{u_c} \sqrt{1 - \left(\frac{u}{u_c}\right)^2} \right], \quad (7)$$

and $\mathcal{A} = 2/(\pi^4 d^2)$, $u \equiv \frac{k}{2\pi}$. The diameter of the telescope, d , is taken to be 6 m. If the characteristic maximum opening of the telescope is θ (set to be 70°), then $u_c = \theta/\lambda$ with λ being the wavelength of the observation. Eq. 7 defines $\tilde{A}(u)$ only for $u \leq u_c$ and $\tilde{A}(u)$ is zero elsewhere. The normalization guarantees that $A(0) = 1$. In the small-scale regime, the multipole representation of Eq. 7 is

$$\tilde{A}(\ell) = \mathcal{A} \left[\arccos \frac{\ell}{\ell_c} - \frac{\ell}{\ell_c} \sqrt{1 - \left(\frac{\ell}{\ell_c}\right)^2} \right], \quad (8)$$

where $\ell_c = 2\pi d/(\lambda\theta)$. The suppressing effect of the beam on large multipoles is evident from Figure 1. The dotted line represents the beamed power spectrum of CMB fluctuations whereas the dashed-dot-dot line corresponds to the underlying temperature distribution on the sky. This smearing effect is also recognizable on the map itself for small scales (see Figure 2).

3 COSMIC STRING DETECTION PIPELINE

Our goal in this work is to evaluate the performance of various sequences of image-processing and statistical tools in the detection of the trace of a possible CS network on CMB temperature anisotropies. We are interested in detecting line-like discontinuities in temperature maps produced by the strings and curvelets are an adequate tool for this purpose. Indeed, the basis functions of curvelets are localized in both Fourier and position spaces. These elongated basis functions enable curvelets to track well the CS footprints on CMB maps (Fadili & Starck 2009). The maps are then passed through a chain of filters to magnify their edge discontinuities. Statistical measures and a P-value analysis are applied to these curvelet-decomposed and gradient maps to assess the capability of the methods in detecting CSs contribution for the various beam and noise levels associated with each experiment. In brief, our proposed pipeline comprises two major steps:

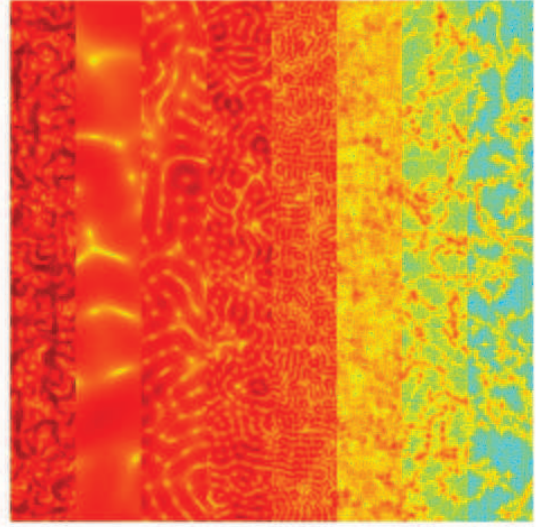


Figure 3. Filtered GSB maps generated from different curvelet components of CMB anisotropies (beam of 0.9'). From left to right, the first panel is the full map, and the rest are the first to the seventh curvelet components. The filter used for edge extraction is *Scharr* (Jain et al. 1995). The CS network contribution to the fluctuations corresponds to $G\mu = 1.0 \times 10^{-7}$. The visual detectability of the string-induced discontinuities, especially in the panels with finer scales (i.e., in the higher curvelet modes) is striking. The color scale is logarithmic.

1– Processing CMB maps: here we apply several image-processors with the aim to isolate or/and enhance the CSs imprint on CMB maps (see Section 3.1). The two pillars of this step are a multi-scaling analysis through curvelet-decomposition of the input maps (Section 3.1.1) and the generation of filtered maps through extended Canny algorithm (ECA) (Section 3.1.2).

2– Analysis of processed CMB maps: here we use various statistical measures to quantify the detectability of CSs signature on the filtered maps from the first step (see Section 3.2).

The efficiency of the method can be summarized by the minimum detectable value of $G\mu$ for each sequence of steps.

3.1 Processing CMB maps

In this section, we develop the image-processing part of our CS detection pipeline with the aim to increase the chances of the CS signal detectability.

3.1.1 Multi-scaling analysis: curvelet decomposition of CMB maps

The expansion of a field or function in a complete set of basis functions has a long history in various fields of study, with the most familiar one known as the Fourier transformation. The basis functions for Fourier transformation are maximally localized in wavenumber (frequency) space. Therefore, the individual Fourier components have no information about local events in position (time) space. To

resolve this limitation, generalizations of Fourier transformations, such as wavelet and ridgelet transforms, have been developed.

Wavelets are developed with localized basis functions in both position (time) and wavenumber (frequency) spaces. They provide an excellent mathematical architecture for sparse representation of data with transient or local features, where too many Fourier modes would otherwise be required. Wavelets accomplish this by using multi-scale, local basis functions which are isotropically extended. In order to assess anisotropic features embedded in the underlying field, additional modification are required. More specifically, the orientation selectivity of wavelet is weak and, in two or three dimensions, can not efficiently represent curve-like singularities. For example, the basic 2D wavelet is not able to identify elongated features such as signature of the CSs as discontinuities along the edges.

Alternative transformations, which are capable of overcoming this limitation, are ridgelets and curvelets, firstly introduced and developed by (Candes & Donoho 2000; Donoho & Duncan 2000; Candès & Donoho 2001). They are relatively new in the wavelet family and are already widely used in various fields from medicine to physics (see (Fadili & Starck 2009) for a comprehensive introduction). Ridgelet transformations take into account scales and positions as well as orientations, and are ideal for straight line detection.

Curvelets, on the other hand, are commonly used when some sort of smooth curve detection is required. Intuitively, the curvelet transform is a multi-scale pyramid with enough directions and positions at each given length scale, and needle-shaped elements at fine scales. Therefore, curvelets decompose two and three dimensional images and data sets into contributions from different scales, locations and directions. They are different from other directional wavelets, such as countourlets and directionlets, in that the degree of directional localization is scale-dependent. This characteristic makes curvelets ideal for sparse representation of images which are smooth except for curve-like discontinuities or edges. The first generation of curvelets (curveletG1), based on local ridgelet transforms, could extract edges in suppressed backgrounds (Donoho & Duncan 2000; Candès & Donoho 2001), with significant improvement in the next version (curveletG2) where a mother (prototype) curvelet function is used for computing the expansion coefficients (Candès & Donoho 2004; Candès & Guo 2002). Using unequally Spaced Fast Fourier Transform, (Candes et al. 2006) developed two fast discrete curvelet transforms which are simpler, faster and more efficient compared to other approaches, and have both discrete and continuous versions

The general curvelet transformation of a square integrable two dimensional map $T \in L^2(\mathbb{R}^2)$ is given by:

$$T(x, y) = \sum_{j,k,l} \langle T, \phi_{jkl} \rangle \phi_{jkl} \quad (9)$$

where the ϕ_{jkl} 's are the curvelet basis functions. The curvelet coefficients, represented by $\langle T, \phi_{jkl} \rangle$ are given by the L^2 -scalar product of the map T and the ϕ_{jkl} 's. The three indices j , k and l represent scale, orientation and location (in position space), respectively. In this work we use *CurveLab*², the 2D discrete version of the curvelet transform. We

0 0 0	0 1 0	-1 0 1	3 0 -3
0 1 -1	1 -4 1	-2 0 2	10 0 -10
0 0 0	0 1 0	-1 0 1	3 0 -3
D_x	\mathcal{L}	G_x	H_x

Figure 4. Different filters for edge recovery applied on the anisotropy maps after curvelet decomposition. Left to right: the standard unit neighborhood derivative in the x direction, the Laplacian operator, the Sobel operator in the x direction and the Scharr operator in x direction. The "y-axis" operators are made similar to "x-axis" with proper rotations.

wrapped the original package in Python, called *Pycurvelet*, which is available upon request.

CurveLab applies the Fast Fourier Transform (FFT) on the data. The resulting 2D Fourier map is then divided into wedges through slicing by concentric circles and angular divisions. This procedure decomposes the map into multiple scales and different orientations. Each wedge, produced this way, corresponds to a certain curvelet component, associated with a particular scale and orientation. Applying inverse FFT on a given wedge leads to the corresponding curvelet coefficient for the associated scale and orientation at a given point.

Among the adjustable parameters used in the decomposition are the number of scales n_{scales} and orientations n_{angles} . Higher values of these parameters correspond to more components and higher resolutions. In the trade-off between the computational cost and the desired accuracy of the results, we found the appropriate parameters for our work to be $n_{\text{scales}} = 7$ and $n_{\text{angles}} = 10$. Figure 3 illustrates the seven curvelet components of a simulated CMB sky with contribution from the CS network with $G\mu = 1.0 \times 10^{-7}$, compared to the full map itself (the leftmost bar). The trace of the CS network is visually distinguishable for components with high mode number.

3.1.2 Filtering the maps: extended Canny algorithm

The imprint of the CS network on CMB anisotropies can be thought of as (the superposition of) line-like structures, conveniently characterized by sharp discontinuities known as edges. Among the widely used algorithms developed to identify edges in 2D images is the Canny edge detector (Canny 1986) which is a multi-stage method. The image is initially smoothed by a Gaussian kernel to reduce the intrinsic noisiness due to the stochastic nature of the field. The edges are defined as points with large gradients. Therefore, the central piece of the algorithm is to find the image gradient.

The edge-identification step of our CS-detection pipeline is based on the Canny algorithm, but is extended in certain ways, and is therefore called the extended Canny algorithm (ECA). The extensions include using kernels other than the Gaussian to smooth the maps, including Boxcar and Hanning (Blackman & Tukey 1958). We also apply various filters, including *Derivative* (der), *Laplacian* (lap), *Sobel* (sob) (Jähne et al. 1999) and *Schaar* (sch) (Jain et al. 1995),

lab and C++ implementations of both the USFFT-based and the wrapping-based transforms.

² Available at <http://www.curvelet.org/>. It contains the *Mat-*

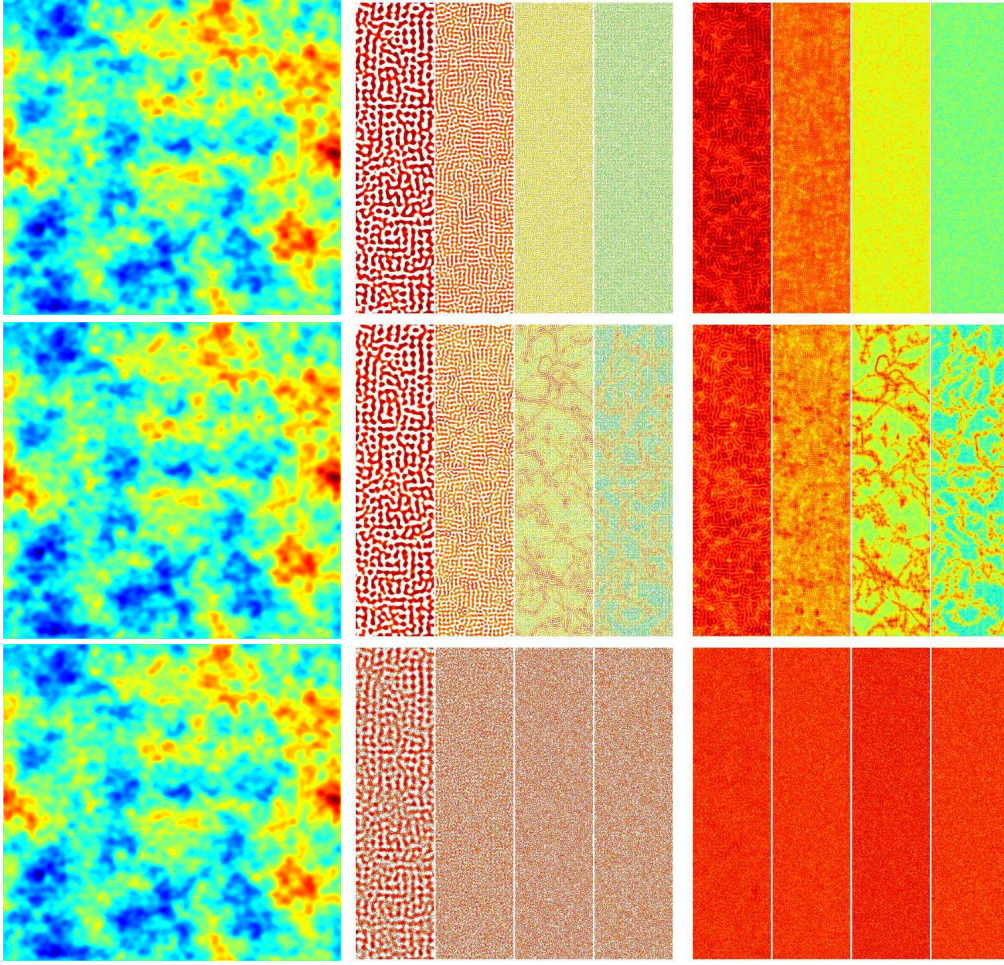


Figure 5. Visual evaluation of the image-processing steps of the proposed CS-detection pipeline. The top, middle and bottom rows correspond respectively to GB maps, GSB maps with $G\mu = 1.0 \times 10^{-7}$, and GSNB maps with $G\mu = 1.0 \times 10^{-7}$ and $SNR = 20$ (similar to the noise level of a CMB-S4 phase II experiment). From left to right, the panels are the full maps, the fourth to the seventh curvlet components and their edge maps produced by *Scharr* filter. The CS trace, not visually distinguishable in the map, is clearly detectable in the last two components, with significantly boosted detectability after filtering.

to produce gradient maps. Figure 4 illustrates how these filters act on the neighboring pixels to construct the gradient map.

Our ultimate goal is to perform the ECA on curvlet components of the CMB anisotropy maps and evaluate their performance in identifying the CS-induced edge-like features. Figure 5 neatly demonstrates how these two successive steps isolate/enhance the sought-after CS signature on the original CMB maps, and thus prepare it to undergo the next step, i.e., statistical analysis. The rows in Figure 5 represent simulations of GB, GSB (with $G\mu = 1.0 \times 10^{-7}$) and GSNB (with $G\mu = 1.0 \times 10^{-7}$ and $SNR = 20$) cases, from top to bottom, respectively. The columns on the other hand, illustrate the image processing steps: the leftmost panel shows the input maps, the middle represents their (forth to seventh) curvlet components, and the rightmost corresponds to the gradient maps produced from these components, using *Scharr* as the ECA filter. The footprints of the CS network are evident in the curvlet components and more vividly in the filtered maps. Adding noise smears out these footprints, making them no longer visually distinguishable. This neces-

sitates developing proper statistical tools for their detection, as we do in the next section. We will also assess the sensitivity of our detection procedure to various filters for different input maps in Section 4.

3.2 Analysis of the processed CMB maps

Applying the preprocessing steps of Section 3.1 on CMB maps increases the detectability of their possible CS signature, first, through keeping only components with the largest contribution from strings, and secondly, by locating the edges, assumed to be induced by the CS network. Equipped with filtered CMB temperature maps, we now turn to the last step of our pipeline, i.e., measuring certain statistical properties of the maps to quantify the detectability of their CS imprint.

3.2.1 Notation

Here we outline some definitions and introduce our notation, used in the rest of the paper. The CMB temperature

anisotropies is a stochastic field, represented by a 2D map $T \in L^2(\mathbb{R}^2)$ which is obtained according to Eq. (3). One can construct a vector \mathcal{A} at each spatial point as:

$$\{\mathcal{A}\} \equiv \{\delta_T, \eta_x, \eta_y, \xi_{xx}, \xi_{yy}, \xi_{xy}\}$$

where δ_T is the *density contrast* of the stochastic field. For the CMB anisotropies here $\delta_T \equiv T$ (temperature fluctuation). We have also defined $\eta_x \equiv \partial\delta_T/\partial x$, $\eta_y \equiv \partial\delta_T/\partial y$ and $\xi_{xy} \equiv \partial^2\delta_T/\partial x\partial y$. In general, \mathcal{A} can be expanded to include higher order derivatives. On the other hand, in certain cases, the first order derivative may suffice to explore the statistical feature one is interested in. For example, studying the crossing statistics only requires the knowledge of the first order derivatives while peak analysis requires the second order as well.

The characteristic function of \mathcal{A} , intimately related to its free energy, is defined by:

$$\mathcal{Z}(\lambda) = \int_{-\infty}^{+\infty} d^6\mathcal{A} \mathcal{P}(\mathcal{A}) e^{i\lambda \cdot \mathcal{A}}, \quad (10)$$

where λ is an array with the same dimension as \mathcal{A} . \mathcal{Z} can be expanded as (Matsubara 2003)

$$\begin{aligned} \mathcal{Z}(\lambda) = & \exp\left(-\frac{1}{2}\lambda^T \cdot \mathcal{C} \cdot \lambda\right) \\ & \times \exp\left[\sum_{j=3}^{\infty} \frac{i^j}{j!} \left(\sum_{\mu_1}^N \sum_{\mu_2}^N \dots \sum_{\mu_j}^N \mathcal{K}_{\mu_1, \mu_2, \dots, \mu_j}^{(j)} \lambda_{\mu_1} \lambda_{\mu_2} \dots \lambda_{\mu_j}\right)\right]. \end{aligned} \quad (11)$$

where $\mathcal{K}_{\mu_1, \mu_2, \dots, \mu_n}^{(n)} \equiv \langle \mathcal{A}_{\mu_1} \mathcal{A}_{\mu_2} \dots \mathcal{A}_{\mu_n} \rangle_c$ are the cumulants and $\langle \rangle_c$ stresses that only *connected* cumulants are taken into account. Here N is the dimension of \mathcal{A} and throughout this paper $N = 6$. Also $\mathcal{C} \equiv \langle \mathcal{A} \otimes \mathcal{A} \rangle$ represents the 6×6 covariance matrix of \mathcal{A} at each spatial point. Note that with the zero-mean CMB fluctuations the cumulants are the same as moments. Various spectral parameters for the CMB field are defined by

$$\begin{aligned} \sigma_m^2 & \equiv \langle \nabla^m \delta_T \nabla^m \delta_T \rangle \\ & = \frac{1}{(2\pi)^2} \int d\mathbf{k} k^{2m} P_{TT}(k) \tilde{W}^2(kL), \end{aligned} \quad (12)$$

for small sky coverage. In this expression, \tilde{W} stands for any smoothing function, such as the beam, and L is the smoothing scale.

3.2.2 Statistical measures

Here we introduce the statistical tools used in this work to quantify the detectability of the imprints left by the CS network on CMB anisotropies.

1– The one-point PDF

The one-point probability density function (hereafter, the PDF) of a distribution describes the statistical abundance of the field values and can be calculated from the inverse Fourier transform of the characteristic function. For the joint probability density function (JPDF) of \mathcal{A} we have

$$\mathcal{P}(\mathcal{A}) = \frac{1}{(2\pi)^6} \int_{-\infty}^{+\infty} d^6\lambda \mathcal{Z}(\lambda) e^{-i\lambda \cdot \mathcal{A}}. \quad (13)$$

Plugging Eq. (11) in Eq. (13) gives

$$\begin{aligned} \mathcal{P}(\mathcal{A}) = & \exp\left[\sum_{j=3}^{\infty} \frac{(-1)^j}{j!} \left(\sum_{\mu_1=1}^6 \dots \sum_{\mu_j=1}^6 \mathcal{K}_{\mu_1, \mu_2, \dots, \mu_j}^{(j)} \right. \right. \\ & \left. \left. \times \frac{\partial^j}{\partial \mathcal{A}_{\mu_1} \dots \partial \mathcal{A}_{\mu_j}}\right)\right] \mathcal{P}_G(\mathcal{A}), \end{aligned} \quad (14)$$

where

$$\mathcal{P}_G(\mathcal{A}) = \frac{1}{\sqrt{(2\pi)^6 |\mathcal{C}|}} e^{-\frac{1}{2}(\mathcal{A}^T \cdot \mathcal{C}^{-1} \cdot \mathcal{A})}. \quad (15)$$

The anisotropies produced by the CS network are non-Gaussian (Ringeval 2010). The perturbative form of the one-point PDF of the temperature fluctuations, $\mathcal{P}_{\delta_T}(\alpha)$, in the presence of CSs, keeping only terms up to $\mathcal{O}(\sigma_0^3)$, is given by

$$\begin{aligned} \mathcal{P}_{\delta_T}(\alpha) & = \langle \delta_d(\delta_T - \alpha) \rangle = \int d^6\mathcal{A} \delta_d(\delta_T - \alpha) \mathcal{P}(\mathcal{A}) \\ & = \frac{1}{\sqrt{2\pi\sigma_0}} e^{-\alpha^2/2\sigma_0^2} [1 + A\sigma_0 + B\sigma_0^2 + \mathcal{O}(\sigma_0^3)]. \end{aligned} \quad (16)$$

Here $A \equiv \frac{S_0}{6} H_3\left(\frac{\alpha}{\sigma_0}\right)$ and $B \equiv \frac{K_0}{24} H_4\left(\frac{\alpha}{\sigma_0}\right) + \frac{S_0^2}{72} H_6\left(\frac{\alpha}{\sigma_0}\right)$. Also $S_0 \equiv \langle \delta_T^3 \rangle_c / \sigma_0^3$ and $K_0 \equiv \langle \delta_T^4 \rangle_c / \sigma_0^4$ are the modified skewness and kurtosis quantities, respectively. The $H_n(\delta_T/\sigma_0)$ represents the probabilistic's Hermite polynomial of order n . Note that the $G\mu$ levels we are interested in have tiny contributions to the CMB fluctuations compared to inflation-induced anisotropies. However, we show that proper sequences of image-processing and statistical steps can explore these regimes and possibly detect the tiny imprints.

2– The (weighted) TPCF

The (weighted) two-point correlation function (TPCF) is defined as $\mathcal{C}_{TT} = \langle \delta_T(\mathbf{r}_1) \delta_T(\mathbf{r}_2) \rangle$ where \mathbf{r}_1 and \mathbf{r}_2 represent the coordinates of the points. \mathcal{C}_{TT} is another statistical measure we employ in this work to search for possible deviation from the \mathcal{C}_{TT} produced by inflationary anisotropies.

3– The unweighted TPCF of peaks

Topological and geometrical criteria to characterize morphology of cosmological stochastic fields in one, two and three dimensions, have been considered in various researches (see e.g. Matsubara 2003; Ducoat et al. 2013; Pogosyan et al. 2009; Gay et al. 2012; Codis et al. 2013). The clustering of these measures based on their TPCF also provides a useful statistical framework. Here we focus on the local maxima clustering. The unweighted TPCF of a certain feature of a stochastic field, also referred to as its excess probability, is a robust measure of the clustering of that feature. From the statistical-mechanics point of view, the information about an interacting system is encoded in the excess probability of finding certain features of the stochastic field representing that system. In this paper we compare the clustering of the local maxima of CMB maps for Gaussian-only fluctuations with those including contributions from the CS network as well. The excess probability of finding peak pairs $\Psi_{\text{pk-pk}}$ separated by distance $r = |\mathbf{r}_1 - \mathbf{r}_2|$, at thresholds $\vartheta_1 \equiv \alpha_1/\sigma_0$ and $\vartheta_2 \equiv \alpha_2/\sigma_0$ is defined as

$$\Psi_{\text{pk-pk}}(r; \vartheta_1, \vartheta_2) = \frac{\langle n_{\text{pk}}(\mathbf{r}_1, \vartheta_1) n_{\text{pk}}(\mathbf{r}_2, \vartheta_2) \rangle}{\bar{n}_{\text{pk}}(\vartheta_1) \bar{n}_{\text{pk}}(\vartheta_2)} - 1, \quad (17)$$

where $\bar{n}_{\text{pk}}(\vartheta)$ is the number density of peaks and is mathematically given by

$$\bar{n}_{\text{pk}}(\vartheta) = \langle \delta_{\text{d}}(\delta_T - \vartheta\sigma_0)\delta_{\text{d}}(\eta) |\det(\xi)| \rangle, \quad (18)$$

The second derivative tensor of the CMB field (ξ_{ij}) should be *negative definite* at peak position. Its analytical expression for a 2D homogenous Gaussian field was calculated in (Bardeen et al. 1986; Bond & Efstathiou 1987). An estimator for this excess probability, $\tilde{\Psi}_{\text{pk-pk}}(r; \vartheta)$, is given by

$$\tilde{\Psi}_{\text{pk-pk}}(r; \vartheta) = \left[\frac{DD(r, \vartheta)}{RR(r, \vartheta)} \right] \frac{N_R(N_R - 1)}{N_D(N_D - 1)} - 1, \quad (19)$$

which usually reduces the boundary effect (Landy & Szalay 1993). Here, $RR(r, \vartheta)$ and $DD(r, \vartheta)$ are the number of peak pairs in random and data catalogs, respectively, separated by distance r from each other. Similarly, N_D and N_R are the total number of peaks in data and random catalogs, respectively.

4– The unweighted TPCF of up-crossings

The crossing statistics was first introduced by (Rice 1944). Since then, it has been used to study the geometry of stochastic fields in various disciplines, e.g., in complex systems (Brill 2000; Peppin 1994; Jafari et al. 2006; Vahabi et al. 2011), material sciences (Nezhadhighi et al. 2017), optics (Goodman 2007; Yura & Hanson 2010; Pirlar et al. 2017) and cosmology and early universe (Ryden et al. 1989; Ryden 1988; Matsubara 1996; Movahed & Khosravi 2011; Matsubara 2003; Musso & Sheth 2014a,b). Crossing statistics can be introduced for 1, 2 and 3D stochastic fields. For 1D it corresponds to crossing at a given threshold. Length or contour statistics corresponds to crossing statistics for a typical 2D field, while for 3D, area statistics is representative of crossing statistics. To be more specific, to up-cross a given threshold refers to when the field at a point crosses the threshold with a positive slope (in a certain direction in a 2D field). In an isotropic stochastic field, up-crossing and down-crossing (i.e., crossing with a negative slope) are statistically equivalent. The probabilistic framework of the mean number of up-crossings of a 2D field δ_T at a threshold ϑ for an arbitrary 1D slice denoted by \otimes is given by:

$$\bar{n}_{\text{up}}^{\otimes}(\vartheta) = \langle \delta_{\text{d}}(\delta_T - \vartheta\sigma_0)\Theta(\eta^{\otimes}) |\eta^{\otimes}| \rangle, \quad (20)$$

where $\Theta(\eta)$ is the unit step function and $|\eta^{\otimes}|$ is the absolute value of the first derivative of temperature fluctuations in direction \otimes (e.g., see Matsubara 2003). For statistically isotropic CMB map, one can choose any direction \otimes on the map, and work in that direction with the one dimensional notion of the up-crossing, without loss of generality. For a pure Gaussian CMB stochastic field, we have

$$\bar{n}_{\text{up}}^{\otimes}(\vartheta) = \frac{1}{2\pi\sqrt{2}} \frac{\sigma_1}{\sigma_0} e^{-\vartheta^2/2}, \quad (21)$$

where σ_0 and σ_1 are spectral parameters defined by Eq. (12). In this work, we go beyond the one-point statistics of up-crossings, $\bar{n}_{\text{up}}^{\otimes}(\vartheta)$, and investigate their clustering as well, characterized by the excess probability of finding a pair of up-crossings separated by distance $r = |\mathbf{r}_1 - \mathbf{r}_2|$, at thresholds ϑ_1 and ϑ_2

$$\Psi_{\text{up-up}}(r; \vartheta_1, \vartheta_2) = \frac{\langle n_{\text{up}}(\mathbf{r}_1, \vartheta_1)n_{\text{up}}(\mathbf{r}_2, \vartheta_2) \rangle}{\bar{n}_{\text{up}}(\vartheta_1)\bar{n}_{\text{up}}(\vartheta_2)} - 1, \quad (22)$$

where $\bar{n}_{\text{up}}(\vartheta) = \langle \bar{n}_{\text{up}}^{\otimes}(\vartheta) \rangle$ and the averaging is over all

available directions.

5– The unweighted cross-correlation of up-crossings and peaks

We define the cross-correlation of peaks and up-crossings as:

$$\Psi_{\text{up-pk}}(r; \vartheta_1, \vartheta_2) = \frac{\langle n_{\text{up}}(\mathbf{r}_1, \vartheta_1)n_{\text{pk}}(\mathbf{r}_2, \vartheta_2) \rangle}{\bar{n}_{\text{up}}(\vartheta_1)\bar{n}_{\text{pk}}(\vartheta_2)} - 1. \quad (23)$$

3.2.3 Quantifying the CS-induced deviation

In the following, we apply the five statistical measures introduced above on the ECA gradient maps. These are generated through applying various filters on different curvelet components of simulated CMB maps. In order to investigate the detectability of the (enhanced) CS footprints on these gradient maps, we define the following Δ_{\diamond} 's. This quantity enables us to quantify the deviation from pure-inflationary simulations of a certain measure (labeled by \diamond) calculated for maps with different $G\mu$'s. To avoid bias in Δ_{\diamond} , $\mathcal{C}_{TT}(r)$, $\Psi_{\diamond}(r, \vartheta; \times)$ and $\mathcal{P}(\alpha)$ are generated by averaging over 1000 null cases, i.e., with $G\mu = 0$, simulations.

For the PDF and the weighted TPCF, we define

$$\begin{aligned} \Delta_{\text{PDF}}^{\times}(G\mu) &\equiv \int d\alpha |\mathcal{P}(\alpha; \times; G\mu) - \mathcal{P}(\alpha; \times; G\mu = 0)|, \\ \Delta_{\text{TT}}^{\times}(G\mu) &\equiv \int dr |C_{TT}(r; \times; G\mu) - C_{TT}(r; \times; G\mu = 0)|. \end{aligned} \quad (24)$$

The symbol \times represents the specific sequence of curvelet component and ECA filter being used. Also $\alpha \equiv \vartheta\sigma_0$. For the TPCF we define

$$\Delta_{\diamond}^{\times}(G\mu) \equiv \sum_{\vartheta} \int dr |\Psi_{\diamond}(r, \vartheta; \times; G\mu) - \Psi_{\diamond}(r, \vartheta; \times; G\mu = 0)|. \quad (25)$$

Here " \diamond " can be "pk-pk", "up-up" or "up-pk".

Finally we can compare simulations with string-induced fluctuations with null sets. In the next section we will present our results by reporting the minimum detectable value of $G\mu$ in CMB observations for various noise levels, using different parameter settings in the proposed pipeline.

4 RESULTS

In this section, we present the results of the above pipeline applied to CMB simulations with varying levels of CS contribution, different beam resolutions and various experimental noise levels. Sections 4.1 and 4.2 investigate noise-free and more realistic cases, respectively.

The curvelet decomposition step of our algorithm (Section 3.1.1) provides us with four maps, $n_{\text{curvelet}} = 4$: the map itself, and the last three (i.e., the fifth to the seventh) curvelet components. In the ECA step (Section 3.1.2) we use $n_{\text{filter}} = 5$ filters for edge extraction, corresponding

to four differentiation schemes and a case with no filtering at all. Finally, applying different statistical tools (Section 3.2.1) on a single gradient map for a given curvelet component gives $n_{\text{statistics}} = 5$ measures $\Delta_{\diamond}^{\times}(G\mu)$. Thus, there are $n_{\text{curvelet}} \times n_{\text{filter}} \times n_{\text{statistics}} = 100$ different combinations of image-processing and statistical settings to be used in our pipeline.

In order to quantify the capability of the pipeline in detecting CSs, we estimate the statistical difference of $\Delta^{\times}(G\mu)$ and $\Delta^{\times}(G\mu = 0)$ (corresponds to a map with no CS network). The significance of this deviation is systematically checked by computing the Student's t-test for equal sample sizes and unequal means and variances as

$$t_{\text{PDF}}^{\times}(G\mu) = \left[\overline{\Delta_{\text{PDF}}^{\times}}(G\mu) - \overline{\Delta_{\text{PDF}}^{\times}}(G\mu = 0) \right] \sqrt{\frac{N_{\text{sim}}}{[\sigma_{\text{PDF}}^{\times}(G\mu)]^2 + [\sigma_{\text{PDF}}^{\times}(G\mu = 0)]^2}}, \quad (26)$$

$$t_{\text{TT}}^{\times}(G\mu) = \left[\overline{\Delta_{\text{TT}}^{\times}}(G\mu) - \overline{\Delta_{\text{TT}}^{\times}}(G\mu = 0) \right] \sqrt{\frac{N_{\text{sim}}}{[\sigma_{\text{TT}}^{\times}(G\mu)]^2 + [\sigma_{\text{TT}}^{\times}(G\mu = 0)]^2}}, \quad (27)$$

$$t_{\diamond}^{\times}(G\mu) = \left[\overline{\Delta_{\diamond}^{\times}}(G\mu) - \overline{\Delta_{\diamond}^{\times}}(G\mu = 0) \right] \sqrt{\frac{N_{\text{sim}}}{[\sigma_{\diamond}^{\times}(G\mu)]^2 + [\sigma_{\diamond}^{\times}(G\mu = 0)]^2}}, \quad (28)$$

where σ is the standard deviation, N_{sim} is the number of simulations and $\overline{\Delta^{\times}}$ denotes the mean value of Δ^{\times} over the N_{sim} maps.

We finally calculate the P-value statistics for the above Student's t-test and determine the P-value as a function of $G\mu$ for all parameter settings in the pipeline. In the following, the minimum detectable $G\mu$, denoted by $G\mu_{\text{min}}$, refers to the $G\mu$ whose P-value is smaller than a given threshold. We take this threshold to be 0.0027, corresponding to the 3σ frequentist level.

4.1 Ideal Case

We apply our proposed CS-detection pipeline in all its different parameter settings, explained in Section 3, to noise-free simulated CMB skies with various levels of CS contributions. Our ideal experiment corresponds to a noise free CMB sky convolved with the beam of an ACT-like telescope.

More specifically, we construct different gradient maps of various curvelet components of the GB and GSB maps, and then compare some of their statistical properties using the measures outlined earlier. In the following we report, for any given statistical measure, the lowest $G\mu_{\text{min}}$ and its corresponding parameter setting (i.e., curvelet component and ECA filter). Table 1 summarizes the results.

1) With Δ_{PDF} as the measure, we find that applying the *Laplacian* filter in the ECA step on the seventh curvelet component gives the best detection of the CS signature. We conclude that, in the absence of instrumental noise and foreground contamination, our proposed method is basically capable of robustly detecting the imprints of CSs with string tension $G\mu \gtrsim 4.3 \times 10^{-10}$ using the *c7-Laplacian- Δ_{PDF}* sequence.

2) With Δ_{TT} as the measure, we find that applying the *Sobel* filter on the seventh curvelet component results in the best CS detection. This sequence of steps is able to discriminate maps with contributions from CSs with $G\mu \gtrsim 2.3 \times 10^{-9}$ from null sky maps.

3) With $\Delta_{\text{pk-pk}}$ as the measure, we find that applying the *Laplacian* filter on the fifth component yields the best

detection of the CS contribution, setting the lower detection bound of $G\mu \gtrsim 8.7 \times 10^{-10}$.

4) With $\Delta_{\text{up-up}}$ as the measure, we find that the seventh curvelet component and the *Derivative* filter are most sensitive to the CS signature, giving $G\mu \gtrsim 8.5 \times 10^{-10}$.

5) Finally with $\Delta_{\text{up-pk}}$ as the measure, we conclude that applying the *Derivative* filter on the seventh curvelet component gives the best detection for CSs, able to detect strings with tensions $G\mu \gtrsim 8.7 \times 10^{-10}$.

In the next section we investigate the performance of the pipeline in more realistic scenarios by including both the instrumental noise and beam resolution of current and future CMB experiments.

4.2 Realistic Case

In the previous section, we investigated the performance of our proposed CS-detection pipeline for simulations of ideal CMB observations. Now we take into account noise contamination as explained in Section 2.3. It turns out that, unlike the ideal case, the role of the curvelet decomposition becomes less significant as the noise level increases. Also, the scale of the best curvelet component for CS detection depends on the noise level. Table 1 summarizes the results of our search for $G\mu_{\text{min}}$ in these experimental setups, and presents the optimum pipeline settings for best CS signal recovery using various statistical measures. One may note that some experimental setups are not present in the table, e.g., the ACT-like case with Δ_{TT} . This is because for these cases, and for a given beam, the minimum detectable value of $G\mu$ is weaker than the explored range. For an ACT-like telescope, this corresponds to $G\mu_{\text{min}} \gtrsim 5 \times 10^{-7}$.

Our results are commented below according to the considered statistical measure.

1) Using the measure Δ_{PDF} .

For an ACT-like instrumental noise level, CSs are detectable with tensions $G\mu \gtrsim 1.3 \times 10^{-7}$ with *Scharr*-filtered maps. For CMB-S4 phase I- and II-like noise levels, the minimum detectability slightly improves to $G\mu \gtrsim 1.2 \times 10^{-7}$ for the *Scharr*-filtered map and the *Scharr*-filtered fifth

component, respectively. For a *Planck*-like case one gets $G\mu \gtrsim 4.8 \times 10^{-7}$ with the *Scharr*-filtered sixth component.

2) Using Δ_{TT} as the criterion.

For a CMB-S4 phase I-like noise level, we get the lower bound $G\mu \gtrsim 5.0 \times 10^{-7}$, from the *Sobel*-filtered fifth components. For a CMB-S4 phase II-like noise level, the fifth component itself (with no filtering) yields the best detectability with $G\mu \gtrsim 4.9 \times 10^{-7}$. The lower bound for a *Planck*-like experiment would be $G\mu \gtrsim 9.4 \times 10^{-7}$, using the *Sobel*-filtered fifth component.

3) For $\Delta_{\text{pk-pk}}$, the results are as follows.

For CMB-S4 phase I- and II-like noise levels, using the *Sobel*-filtered fifth and sixth components shows that CSs with tensions $G\mu \gtrsim 5.0 \times 10^{-7}$ and $G\mu \gtrsim 4.8 \times 10^{-7}$ are respectively detectable. While for a *Planck*-like experimental setup would reduce this string detectability to $G\mu \gtrsim 8.9 \times 10^{-7}$ obtained through applying the *Laplacian* filter on the map itself.

4) Using $\Delta_{\text{up-up}}$ as the statistical criterion.

For an ACT-like noise level, the minimum detectability is $G\mu \gtrsim 4.9 \times 10^{-7}$, corresponding to *Scharr*-filtered fifth component. With CMB-S4 phase I- and phase II-like noise levels, using the *Sobel*-filters on the map and on the fifth component yields the minimum detectability of $G\mu \gtrsim 4.9 \times 10^{-7}$ and $G\mu \gtrsim 2.4 \times 10^{-7}$, respectively. The minimum detectability corresponding to the *Planck*-like observational scenario in this case is provided by the *Sobel*-filtered fifth component to be $G\mu \gtrsim 8.4 \times 10^{-7}$.

5) Using the measure $\Delta_{\text{up-pk}}$.

For the CMB-S4 phase I-like noise level, using the *Scharr*-filtered map gives $G\mu \gtrsim 5.0 \times 10^{-7}$, improving to $G\mu \gtrsim 2.4 \times 10^{-7}$ for the CMB-S4 phase II-like noise level with the use of the *Sobel*-filtered fifth component.

5 SUMMARY AND CONCLUSIONS

Increasing the quantity and quality of observational data provides the opportunity to search for possible features present in beyond-the-standard models. A well-motivated example is the CS network, possibly produced in a series of symmetry breaking phase transitions in the very early Universe. If such a network exists, CMB anisotropies are among the powerful observational data sets for their discovery. However, finite instrumental noise and beam smearing effect greatly reduce the detectability of their trace.

Our purpose in this work was to exploit the specific anisotropy patterns, especially the line-like discontinuities, induced by the CSs on the CMB temperature maps, to enhance the string network detectability. Therefore, we have tested a multi-step pipeline which employs image-processing tools to amplify the string signal as well as statistical measures to quantify the deviation of the simulated data from pure Gaussian inflation-induced anisotropies.

The first image-processing step is a curvelet decomposition, an appropriate tool for the detection of elongated sharp edges. As a result, it isolates the components with the highest string contribution. The second image-processing step is based on the extended Canny algorithm, and produces gradient (or filtered) maps with magnified string signatures. The gradient maps are then passed to the statistical unit of the pipeline to investigate the detectability of the strings with

Table 1. Lowest detectable $G\mu$, labeled as $G\mu_{\text{min}}$, of the CSs network superimposed on the CMB map, using various statistical measures. The first column, "Measure", contains the probability density function (PDF), the correlation function of temperature fluctuations versus angle separation (TT), the unweighted TPCF of local maxima (pk-pk), the unweighted TPCF of up-crossings (up-up) and the unweighted cross-correlation of up-crossings and peaks (up-pk). The "Method" corresponds to the sequence of curvelet and ECA filters leading to the best CS detection for the given statistical measure. The "Map" and "FWHM" characterize the experimental setup. CMB-S4-like (I) and (II) represent the phases I and II of a CMB-S4-like experiment, respectively.

Measure	Method	Map	FWHM	$G\mu_{\text{min}}$
PDF	c7-lap	No noise	0.9'	4.3×10^{-10}
	c5-sch	CMB-S4-like (II)	0.9'	1.2×10^{-7}
	map-sch	CMB-S4-like (I)	0.9'	1.2×10^{-7}
	map-sch	ACT-like	0.9'	1.3×10^{-7}
	c6-sch	<i>Planck</i>	5'	4.8×10^{-7}
TT	c7-sob	No noise	0.9'	2.3×10^{-9}
	c5-none	CMB-S4-like (II)	0.9'	4.9×10^{-7}
	c5-sob	CMB-S4-like (I)	0.9'	5.0×10^{-7}
	c5-sob	<i>Planck</i>	5'	9.4×10^{-7}
pk-pk	c5-lap	No noise	0.9'	8.7×10^{-10}
	c6-sob	CMB-S4-like (II)	0.9'	4.8×10^{-7}
	c5-sob	CMB-S4-like (I)	0.9'	5.0×10^{-7}
	map-lap	<i>Planck</i>	5'	8.9×10^{-7}
up-up	c7-der	No noise	0.9'	8.5×10^{-10}
	c5-sob	CMB-S4-like (II)	0.9'	2.4×10^{-7}
	map-sob	CMB-S4-like (I)	0.9'	4.9×10^{-7}
	c5-sch	ACT-like	0.9'	4.9×10^{-7}
	c5-sob	<i>Planck</i>	5'	8.4×10^{-7}
up-pk	c7-der	No noise	0.9'	8.7×10^{-10}
	c5-sob	CMB-S4-like (II)	0.9'	2.4×10^{-7}
	map-sch	CMB-S4 (I)-like	0.9'	5.0×10^{-7}

different $G\mu$ values, thereby enabling us to compare the efficiency of the various settings in the pipeline. These settings, or degrees of freedom, correspond to the various available options for curvelet decomposition, ECA filtering and statistical measures. The pipeline explores the space of these parameters and finds the setting which best constrains the contribution of the string network to the CMB anisotropies. This parameter set depends on the experiment characterization, such as beam and noise level.

We have found that, the curvelet components describing the smaller scales are preferred by the algorithm. This is expected given the small scale nature of the kicks produced by the CSs in the data. In our analysis, this small scale mode corresponds to the seventh mode for an ideal experiment. In the presence of instrumental noise, however, the scale where the CS signal dominates the small-scale noise contamination depends on the noise level. Therefore, the best curvelet component also varies according to the experimental set-up. It also turns out that the two-point statistics, being relatively powerful for an ideal experiment, get highly contaminated by instrumental noise. In these situations, the PDF is the

preferred statistical measure while the results end up being relatively insensitive to the choice of the filter.

For the most efficient pipelines, we could detect the imprints of CS network with tensions as low as $G\mu_{\min} = 4.3 \times 10^{-10}$ for a noise-free experiment having a beam of $\text{FWHM} = 0.9'$. The sequence of pipeline parameter for this case is the seventh curvelet component, the *Laplacian* filter and the one point PDF as the statistical measure (or, $c7 - \text{Laplacian-PDF}$). Including more realistic noise levels increases this minimum detectable tension to $G\mu_{\min} = 1.3 \times 10^{-7}$ and $G\mu_{\min} = 1.2 \times 10^{-7}$ for ACT-like and CMB-S4-like noise levels, respectively, both with a beam pattern described in Section 2.3. All results are listed in Table 1.

We have also considered the unweighted TPCF of up-pk. For noise-free case, we have found $G\mu \gtrsim 8.7 \times 10^{-10}$ for $c7 - \text{Derivative}$ method. Based on the CMB-S4 phase II observational strategy, this type of cross-correlation resulted in $G\mu \gtrsim 2.4 \times 10^{-7}$ for $c5 - \text{Sobel}$.

As a final remark, let us notice that the free parameters selected in this work are by no means exclusive, and should be merely considered as starting points. An obvious extension of the work would thus be to include other statistical measures, which could be possibly more sensitive to CS imprints, and explore other filters to assess their performance in edge detection. One could use deep-learning approaches toward systematic decision making to choose most sensitive features for the CS network detection. This work is in progress. Another possible improvement on our work would be to perform Bayesian model comparison between the best pipelines obtained here on $G\mu$ on real data in order to extract the tightest bound.

ACKNOWLEDGEMENTS

The numerical simulations were carried out on Baobab at the computing cluster of the University of Geneva.

REFERENCES

- Ade P. A. R., et al., 2014, *Astron. Astrophys.*, 571, A25
Ade P. A. R., et al., 2016, *Astron. Astrophys.*, 594, A13
Aghanim N., et al., 2016, *Astron. Astrophys.*, 594, A11
Albrecht A., Battye R. A., Robinson J., 1997, *Phys. Rev. Lett.*, 79, 4736
Allen B., Caldwell R. R., Dodelson S., Knox L., Shellard E. P. S., Stebbins A., 1997, *Phys. Rev. Lett.*, 79, 2624
Amsel S., Berger J., Brandenberger R. H., 2008, *JCAP*, 0804, 015
Bardeen J. M., Bond J. R., Kaiser N., Szalay A. S., 1986, *Astrophys. J.*, 304, 15
Battye R., Moss A., 2010, *Phys. Rev.*, D82, 023521
Bennett D. P., Bouchet F. R., 1988, *Phys. Rev. Lett.*, 60, 257
Bennett D. P., Bouchet F. R., 1989, *Phys. Rev. Lett.*, 63, 2776
Bennett D. P., Bouchet F. R., 1990, *Phys. Rev.*, D41, 2408
Bevis N., Hindmarsh M., Kunz M., Urrestilla J., 2007, *Phys. Rev.*, D75, 065015
Bevis N., Hindmarsh M., Kunz M., Urrestilla J., 2008, *Phys. Rev. Lett.*, 100, 021301
Bevis N., Hindmarsh M., Kunz M., Urrestilla J., 2010, *Phys. Rev.*, D82, 065004
Blackman R. B., Tukey J. W., 1958, *Bell Labs Technical Journal*, 37, 185
Blanco-Pillado J. J., Olum K. D., 2017
Blanco-Pillado J. J., Olum K. D., Shlaer B., 2011, *Phys. Rev.*, D83, 083514
Blanco-Pillado J. J., Olum K. D., Siemens X., 2017
Bond J. R., Efstathiou G., 1987, *Mon. Not. Roy. Astron. Soc.*, 226, 655
Bouchet F. R., Bennett D. P., Stebbins A., 1988, *Nature*, 335, 410
Brandenberger R. H., Danos R. J., Hernandez O. F., Holder G. P., 2010, *JCAP*, 1012, 028
Brill P. H., 2000, *CORS Bulletin*, 34, 9
Candes E. J., Donoho D. L., 2000, Technical report, Curvelets: A surprisingly effective nonadaptive representation for objects with edges. DTIC Document
Candès E. J., Donoho D. L., 2001, *Journal of Approximation Theory*, 113, 59
Candès E. J., Donoho D. L., 2004, *Communications on pure and applied mathematics*, 57, 219
Candès E. J., Guo F., 2002, *Signal Processing*, 82, 1519
Candes E., Demanet L., Donoho D., Ying L., 2006, *Multiscale Modeling & Simulation*, 5, 861
Canny J., 1986, *IEEE Transactions on pattern analysis and machine intelligence*, pp 679–698
Charnock T., Avgoustidis A., Copeland E. J., Moss A., 2016, *Phys. Rev.*, D93, 123503
Christiansen J. L., Albin E., Fletcher T., Goldman J., Teng I. P. W., Foley M., Smoot G. F., 2011, *Phys. Rev.*, D83, 122004
Ciuca R., Hernández O. F., 2017
Codis S., Pichon C., Pogosyan D., Bernardeau F., Matsubara T., 2013, *Mon. Not. Roy. Astron. Soc.*, 435, 531
Contaldi C., Hindmarsh M., Magueijo J., 1999, *Phys. Rev. Lett.*, 82, 679
Copeland E. J., Kibble T. W. B., 2010, *Proc. Roy. Soc. Lond.*, A466, 623
Copeland E. J., Liddle A. R., Lyth D. H., Stewart E. D., Wands D., 1994, *Phys. Rev.*, D49, 6410
Copeland E. J., Myers R. C., Polchinski J., 2004, *JHEP*, 06, 013
Damour T., Vilenkin A., 2005, *Phys. Rev.*, D71, 063510
Danos R. J., Brandenberger R. H., 2010, *Int. J. Mod. Phys.*, D19, 183
Depies M. R., 2009, PhD thesis, Washington U., Seattle, Astron. Dept. ([arXiv:0908.3680](https://arxiv.org/abs/0908.3680)), <https://inspirehep.net/record/829491/files/arXiv:0908.3680.pdf>
Donoho D. L., Duncan M. R., 2000, in *AeroSense 2000*. pp 12–30
Ducout A., Bouchet F., Colombi S., Pogosyan D., Prunet S., 2013, *Mon. Not. Roy. Astron. Soc.*, 429, 2104
Dvali G., Vilenkin A., 2004, *JCAP*, 0403, 010
Fadili J., Starck J.-L., 2009, in *Encyclopedia of Complexity and Systems Science*. Springer, pp 1718–1738
Firouzjahi H., Tye S. H. H., 2005, *JCAP*, 0503, 009
Fraisse A. A., Ringeval C., Spergel D. N., Bouchet F. R., 2008, *Phys. Rev.*, D78, 043535
Gay C., Pichon C., Pogosyan D., 2012, *Phys. Rev.*, D85, 023011
Goodman J. W., 2007, *Speckle phenomena in optics: theory and applications*. Roberts and Company Publishers
Gott III J. R., 1985, *ApJ*, 288, 422
Guth A. H., 1981, *Phys. Rev.*, D23, 347
Hammond D. K., Wiaux Y., Vanderghynst P., 2009, *Mon. Not. Roy. Astron. Soc.*, 398, 1317
Heavens A. F., Sheth R. K., 1999, *Mon. Not. Roy. Astron. Soc.*, 310, 1062
Henry Tye S. H., 2008, *Lect. Notes Phys.*, 737, 949
Hergt L., Amara A., Brandenberger R., Kacprzak T., Refregier A., 2016
Hernandez O. F., Brandenberger R. H., 2012, *JCAP*, 1207, 032
Hernandez O. F., Wang Y., Brandenberger R., Fong J., 2011, *JCAP*, 1108, 014
Hindmarsh M., 1994, *Astrophys. J.*, 431, 534
Hindmarsh M. B., Kibble T. W. B., 1995, *Rept. Prog. Phys.*, 58, 477

- Hindmarsh M., Ringeval C., Suyama T., 2009, *Phys. Rev.*, D80, 083501
- Hindmarsh M., Ringeval C., Suyama T., 2010, *Phys. Rev.*, D81, 063505
- Hinshaw G., et al., 2013, *Astrophys. J. Suppl.*, 208, 19
- Jafari G., Movahed M. S., Fazeli S., Tabar M. R. R., Masoudi S., 2006, *Journal of Statistical Mechanics: Theory and Experiment*, 2006, P06008
- Jähne B., Haussecker H., Geissler P., 1999, *Handbook of computer vision and applications*. Vol. 2, Academic Press San Diego
- Jain R., Kasturi R., Schunck B. G., 1995, *Machine vision*. Vol. 5, McGraw-Hill New York
- Jenet F. A., et al., 2006, *Astrophys. J.*, 653, 1571
- Jeong E., Smoot G. F., 2005, *Astrophys. J.*, 624, 21
- Kaiser N., Stebbins A., 1984, *Nature*, 310, 391
- Kasuya S., Kawasaki M., 2000, *Phys. Rev.*, D61, 083510
- Kibble T. W. B., 1976, *J. Phys.*, A9, 1387
- Kibble T. W. B., 1980, *Phys. Rept.*, 67, 183
- Kibble T. W. B., 2004, in *COSLAB 2004 Ambleside, Cumbria, United Kingdom, September 10-17, 2004*. ([arXiv:astro-ph/0410073](https://arxiv.org/abs/astro-ph/0410073))
- Kuroyanagi S., Miyamoto K., Sekiguchi T., Takahashi K., Silk J., 2013, *Phys. Rev.*, D87, 023522
- Landriau M., Shellard E. P. S., 2003, *Phys. Rev.*, D67, 103512
- Landriau M., Shellard E. P. S., 2004, *Phys. Rev.*, D69, 023003
- Landy S. D., Szalay A. S., 1993, *Astrophys. J.*, 412, 64
- Lazanu A., Shellard P., 2015, *JCAP*, 1502, 024
- Lewis A., Challinor A., Lasenby A., 2000, *Astrophys. J.*, 538, 473
- Liddle A. R., 1999, in *Proceedings, Summer School in High-energy physics and cosmology: Trieste, Italy, June 29-July 17, 1998*. pp 260–295 ([arXiv:astro-ph/9901124](https://arxiv.org/abs/astro-ph/9901124)), <http://alice.cern.ch/format/showfull?sysnb=0301651>
- Liddle A. R., Lyth D. H., 1993, *Phys. Rept.*, 231, 1
- Majumdar M., Christine-Davis A., 2002, *JHEP*, 03, 006
- Matsubara T., 1996, *Astrophys. J.*, 457, 13
- Matsubara T., 2003, *Astrophys. J.*, 584, 1
- McEwen J. D., Feeney S. M., Peiris H. V., Wiaux Y., Ringeval C., Bouchet F. R., 2016
- Moessner R., Perivolaropoulos L., Brandenberger R. H., 1994, *Astrophys. J.*, 425, 365
- Moore J. N., Shellard E. P. S., Martins C. J. A. P., 2002, *Phys. Rev.*, D65, 023503
- Movahed M. S., Khosravi S., 2011, *JCAP*, 1103, 012
- Movahed M. S., Javanmardi B., Sheth R. K., 2012, *Mon. Not. Roy. Astron. Soc.*, 434, 3597
- Musso M., Sheth R. K., 2014a, *Mon. Not. Roy. Astron. Soc.*, 438, 2683
- Musso M., Sheth R. K., 2014b, *Mon. Not. Roy. Astron. Soc.*, 443, 1601
- Nezhadhighi M. G., Movahed S., Yasseri T., Allaei S., 2017, *Journal of Applied Physics*, p. 085302
- Oknyanskij V. L., 2002, *ASP Conf. Ser.*, 282, 352
- Pagano M., Brandenberger R., 2012, *JCAP*, 1205, 014
- Pen U.-L., Seljak U., Turok N., 1997, *Phys. Rev. Lett.*, 79, 1611
- Peppin R. J., 1994, *An Introduction to Random Vibrations, Spectral and Wavelet Analysis*
- Perivolaropoulos L., 1993a, *Phys. Rev.*, D48, 1530
- Perivolaropoulos L., 1993b, *Phys. Lett.*, B298, 305
- Pirlar M. A., Movahed S., Razzaghi D., Karimzadeh R., 2017, *Journal of the Optical Society of America A*, 34, 1620
- Pogosian L., Vachaspati T., 1999, *Phys. Rev.*, D60, 083504
- Pogosian L., Tye S. H. H., Wasserman I., Wyman M., 2003, *Phys. Rev.*, D68, 023506
- Pogosian L., Wasserman I., Wyman M., 2006
- Pogosyan D., Pichon C., Gay C., Prunet S., Cardoso J. F., Sousbie T., Colombi S., 2009, *Mon. Not. Roy. Astron. Soc.*, 396, 635
- Polchinski J., 2005, *Int. J. Mod. Phys.*, A20, 3413
- Pshirkov M. S., Tuntsov A. V., 2010, *Phys. Rev.*, D81, 083519
- Regan D., Hindmarsh M., 2015, *JCAP*, 1510, 030
- Rice S. O., 1944, *Bell Labs Technical Journal*, 23, 282
- Ringeval C., 2010, *Adv. Astron.*, 2010, 380507
- Ringeval C., Bouchet F. R., 2012, *Phys. Rev.*, D86, 023513
- Ringeval C., Suyama T., 2017
- Ringeval C., Sakellariadou M., Bouchet F., 2007, *JCAP*, 0702, 023
- Ryden B. S., 1988, *The Astrophysical Journal*, 333, 78
- Ryden B. S., Melott A. L., Craig D. A., Gott III J. R., Weinberg D. H., Scherrer R. J., Bhavsar S. P., Miller J. M., 1989, *Astrophys. J.*, 340, 647
- Sakellariadou M., 1997, *Int. J. Theor. Phys.*, 36, 2503
- Sakellariadou M., 2007, *Lect. Notes Phys.*, 718, 247
- Sarangi S., Tye S. H. H., 2002, *Phys. Lett.*, B536, 185
- Shellard E. P. S., 1987, *Nucl. Phys.*, B283, 624
- Shlaer B., Vilenkin A., Loeb A., 2012, *JCAP*, 1205, 026
- Stebbins A., 1988, *Astrophys. J.*, 327, 584
- Stebbins A., Veeraraghavan S., 1995, *Phys. Rev.*, D51, 1465
- Steinhardt P. J., 1995, in *Particle and nuclear astrophysics and cosmology in the next millennium. Proceedings, Summer Study, Snowmass, USA, June 29-July 14, 1994*. pp 51–72 ([arXiv:astro-ph/9502024](https://arxiv.org/abs/astro-ph/9502024))
- Stewart A., Brandenberger R., 2009, *JCAP*, 0902, 009
- Tuntsov A. V., Pshirkov M. S., 2010, *Phys. Rev.*, D81, 063523
- Vachaspati T., Vilenkin A., 1984, *Phys. Rev.*, D30, 2036
- Vahabi M., Jafari G., Movahed M. S., 2011, *Journal of Statistical Mechanics: Theory and Experiment*, 2011, P11021
- Vilenkin A., 1981, *Phys. Rev. Lett.*, 46, 1169
- Vilenkin A., 1985, *Phys. Rept.*, 121, 263
- Vilenkin A., Shellard E. P. S., 2000, *Cosmic Strings and Other Topological Defects*. Cambridge University Press, <http://www.cambridge.org/mw/academic/subjects/physics/theoretical-physics-and-mathematical-physics/cosmic-strings-and-other-topological-defects?format=PB>
- Vincent G., Antunes N. D., Hindmarsh M., 1998, *Phys. Rev. Lett.*, 80, 2277
- White M. J., Carlstrom J. E., Dragovan M., 1999, *Astrophys. J.*, 514, 12
- Yura H. T., Hanson S. G., 2010, *JOSA A*, 27, 797
- Zeldovich Ya. B., 1980, *Mon. Not. Roy. Astron. Soc.*, 192, 663

This paper has been typeset from a $\text{\TeX}/\text{\LaTeX}$ file prepared by the author.